



# Experimental Investigation of Soot Production and Oxidation in a Lab-Scale Rich–Quench–Lean (RQL) Burner

Ingrid El Helou<sup>1</sup> · Aaron W. Skiba<sup>1</sup> · Epaminondas Mastorakos<sup>1</sup>

Received: 25 November 2019 / Accepted: 12 February 2020 / Published online: 2 March 2020  
© The Author(s) 2020

## Abstract

Swirl-stabilized, turbulent, non-premixed ethylene–air flames at atmospheric pressure with downstream radially-injected dilution air were investigated from the perspective of soot emissions. The velocity and location of the dilution air jets were systematically varied while the global equivalence ratio was kept constant at 0.3. The employed laser diagnostics included 5 kHz planar laser-induced fluorescence (PLIF) of OH, 10 Hz PAH-PLIF, and 10 Hz laser-induced incandescence (LII) imaging of soot particles. OH-PLIF images showed that the reaction zone widens with dilution, and that regions with high OH-LIF signal shift from the shear layer to the axis of the burner as dilution increases. Dilution is effective at mitigating soot formation within the central recirculation zone (CRZ), as evident by the smaller PAH-containing regions and the much weaker LII signal. Dilution is also effective at halting PAH and soot propagation downstream of the dilution air injection point. The high momentum dilution air circulates upstream to the root of the flame and reduces fuel penetration lengths, induces fast mixing, and increases velocities within the CRZ. Soot intermittency increased with high dilution velocities and dilution jet distances up to two bluff body diameters from the burner inlet, with detection probabilities of < 5% compared to 50% without dilution. These results reveal that soot formation and oxidation within the RQL are dependant on the amount and location of dilution air injected. This data can be used to validate turbulent combustion models for soot.

**Keywords** Soot formation and oxidation · Turbulent non-premixed ethylene flames · RQL · LII and PLIF

## 1 Introduction

When fossil fuels are burned, or when natural fires occur, soot and smoke is released into the atmosphere as a result of incomplete combustion (Houghton et al. 2001; Penner et al. 2003). These microscopic airborne particles are responsible for absorbing solar radiation, and thus have a warming effect on the global climate (Houghton et al. 2001; Penner et al. 2003). However, factors other than the effect on global climate need to be taken into

---

✉ Ingrid El Helou  
ie236@cam.ac.uk

<sup>1</sup> Department of Engineering, University of Cambridge, Cambridge CB2 1PZ, UK

account. Research has linked long-term exposure to particulate air pollution with increased cardiopulmonary and lung cancer mortality rates (Pope et al. 2002). Soot particles range in size from coarse  $> 2.5 \mu\text{m}$  to fine  $< 2.5 \mu\text{m}$  (Dockery et al. 1993). Fine particles extend to the nanoparticle scale (1–100 nm), are produced during the combustion of fossil fuels, and pose a greater risk to human health than coarse particles as they can be inhaled more deeply into the lungs (Pope et al. 2002; Dockery et al. 1993; Samet et al. 2000; Katsouyanni et al. 2001; D’Anna 2009a). These smaller particles evade capture by post combustion cleaning devices and must be reduced in the combustion process itself (D’Anna 2009a).

Soot forms as a consequence of fuel-rich flames in a series of complex physical and chemical steps. Extensive work spanning decades has gone into understanding the mechanisms of soot formation from radical formation to particle growth in laminar flames (Michelsen 2017; Bhargava and Westmoreland 1998; Calcote 1981; Homann 1998; Richter and Howard 2000; Frenklach 2002; Wang 2011). We still do not have a comprehensive understanding of soot formation and oxidation due to the complex nature of the chemical and physical reactions that take place during this process (Wang et al. 2019a). These mechanisms provide the foundation for investigating soot formation in practical combustors (Michelsen 2017).

The many methods used in analysing soot formation can be divided into two main groups: ex situ and in situ diagnostics. The former refers to particle sampling for improved structural and morphologic understanding of soot particles; while the latter focuses on particle formation kinetics (D’Anna 2009a). Ex situ measurements can be conducted in various ways to identify size and molecular weight distributions, and evolution of nanoparticles from the exhaust of a sooting flame. The research done using probe measurements has advanced the understanding of soot inception and growth in both diffusion and premixed laminar flames, and how to differentiate soot particles of differing maturity levels (D’Anna 2009a; Sirignano et al. 2018; D’Anna et al. 2009). There is an extensive review provided by D’Anna on all the ex situ techniques available today (D’Anna 2009a). However, ex situ diagnostics are extractive processes that perturb the flow, and the method of extraction can alter the physical and chemical properties of the soot particles so that they are no longer representative of combustion environments. Additionally, probes are most widely used with laminar flames, and while they can be used to measure size distributions in turbulent flames (Boyette et al. 2017), they cannot measure the high levels of spatial and temporal intermittency of soot formation in turbulent flames identified in many studies (Wang et al. 2019a, b; Lammel et al. 2007; Geigle et al. 2019; Stöhr et al. 2019; Geigle et al. 2011, 2013, 2017; Bartos et al. 2017; Qamar et al. 2005, 2009; Mahmoud et al. 2017, 2018; Köhler et al. 2011; Narayanaswamy and Clemens 2013). These techniques can be used as an accompaniment to in situ laser diagnostics that are currently the main diagnostic techniques used to characterize sooting behavior in turbulent flames.

Laser-induced incandescence (LII) is a widely used technique for in-flame soot detection and can be used to estimate soot volume fractions (Shaddix and Smyth 1996; Vander Wal et al. 1997). Shaddix and Smyth (1996) improved the accuracy of quantitative LII results through corrections to extinction experiments that led to improved soot volume fraction estimates (Shaddix and Smyth 1996). The work of Vander Wal et al. (1997) focused on the importance of tracking polycyclic aromatic hydrocarbons (PAHs) through simultaneous planar laser-induced fluorescence (PLIF) and LII. Simultaneous PLIF-LII is necessary for understanding the role of PAHs in the formation of soot and their growth (Vander Wal et al. 1997). The majority of the in situ experiments conducted to date have been on laminar flames, diffusion and premixed. Multiple parameters such as fuel flow rate, flame geometry, and residence times have been shown to have an effect on soot formation (Qamar

et al. 2009; D’Anna et al. 2005; Geigle et al. 2005; Tsurikov et al. 2005; Santoro et al. 1983, 1987; Smyth et al. 1985; Quay et al. 1994; Santoro and Semerjian 1985; Desgroux et al. 2013; Karataş and Gülder 2012; Steinmetz et al. 2016). Current research is guided by understanding the optical properties, morphology, growth and volume fraction of soot and their precursors under practical combustion conditions. Results from fundamental laminar flames provide a foundation for soot understanding, and can be used for the development of chemical models because they are easier to calculate than turbulent flames. The developed optical diagnostics must be applied to turbulent flames in complex burner geometries in order to extend our understanding of soot formation to practically-relevant configurations.

Turbulent flames exhibit spatial and temporal fluctuations not present in laminar flames, as well as shorter residence times that add a level of complexity to soot studies (Wang et al. 2019a, b; Lammel et al. 2007; Geigle et al. 2011, 2013, 2017, 2019; Stöhr et al. 2019; Bartos et al. 2017; Qamar et al. 2005, 2009; Mahmoud et al. 2017, 2018; Köhler et al. 2011; Narayanaswamy and Clemens 2013). Qamar et al. (2005) investigated soot volume fraction in simple jets (SJ), precessing jets (PJ), and bluff body flames (BB). This work revealed that the higher the global mixing rate the lower the soot volume fraction and the maximum instantaneous soot volume fraction. Global mixing rates were highest for BB, lower for SJ, and the lowest for PJ leading to  $PJ > SJ > BB$  soot concentrations (Qamar et al. 2005). They then expanded their work to cover piloted turbulent jet non-premixed flames showing the intermittency of soot, and that turbulence reduces peak soot volume fractions compared to those in laminar flames (Qamar et al. 2009). Mahmoud et al. presented work on non-premixed turbulent jet flames that were operated at different exit strain rates (Mahmoud et al. 2017, 2018). Their work revealed that soot volume fraction is inversely proportional to exit strain rate, but that the location of maximum soot volume fraction is independent of strain rate (Mahmoud et al. 2017, 2018). Köhler et al. (2011) investigated the interaction between turbulence and soot formation on a turbulent ethylene–air jet flame. They showed that soot does not form in a spatially continuous way in turbulent flames, and that the turbulent velocity field affects the spatial location of soot precursors and particles (Köhler et al. 2011). Narayanaswamy and Clemens performed simultaneous velocity and quantitative soot measurements on a turbulent jet in coflow at varying bulk strain rates. As bulk strain rates increase, peak soot volume fractions decrease, and soot filaments change from elongated and continuous, to spotty and intermittent. This work also revealed that soot forms in regions of low velocity, i.e. low local strain rate, stretches as it is transported, and aligns with the local strain field (Narayanaswamy and Clemens 2013). Investigating soot-turbulence interactions revealed that there is a specific velocity/strain rate at which soot is present, and a wider range of velocities where soot is present in lower magnitudes. Three flames at increasing bulk strain rates were tested and revealed a constant preferred strain rate, and thus residence time for soot presence (Narayanaswamy and Clemens 2013). This work highlighted that the time history of composition and temperature as a time scale for soot formation, and velocity fields for the physical location of soot formation are of the utmost importance (Narayanaswamy and Clemens 2013). This is highly important in turbulent flames where local compositions, temperatures, mixing, and velocities fluctuate and influence soot formation.

The rich–quench–lean (RQL) concept has been used extensively in aero-engines (Samuelson 2006). These practical systems utilize swirl-stabilized combustion that lead to the formation of a central recirculation zone (CRZ) (Syred 2006; Syred and Beer 1974). Swirling flows provide benefits such as flame stabilization and increased mixing, and understanding soot formation in these systems is of the utmost importance. Extensive work using laser diagnostics has been done on swirl stabilized, turbulent flames, premixed and

non-premixed, using mostly gaseous fuels with some more recent work looking at liquid fuels (Wang et al. 2019a, b; Stöhr et al. 2019; Geigle et al. 2011, 2013, 2015a, b, 2017; Roussillo et al. 2018). Geigle and coworkers have looked at the effect of equivalence ratio, thermal power, pressure, and secondary air injection on soot formation in swirl stabilized, turbulent non-premixed ethylene–air flames (Stöhr et al. 2019; Geigle et al. 2011, 2013, 2015a, b, 2017). Their work focused on characterizing the flame and understanding soot formation and mitigation through the use of dilution air. They used instantaneous imaging to focus on the intermittent nature of soot and its sensitivity to gas composition, pressure, temperature, equivalence ratio, amount of oxidation air, and flow field effects such as strain and dilution (Geigle et al. 2013). Simultaneous measurements revealed that the distribution of soot and OH changes with the addition of dilution air. Soot no longer propagates downstream in the central recirculation zone (CRZ) where the OH is dispersed due to the dilution air (Geigle et al. 2015b). Recently, their work has focused on soot-turbulence interactions, revealing that soot forms in rich pockets when residence times are favorable, while soot is oxidized by the OH present in the lean zones (Stöhr et al. 2019). While this large body of work examines the effect that dilution air has on oxidizing soot particles there is still a lack of systematic investigations into the effect of the dilution jet location and the flow split (i.e. the velocity of the dilution jets), while keeping the global equivalence ratio ( $\Phi_g$ ) constant, which is one of the objectives of the present paper. Exploring the air split between the primary swirled air and the dilution air, while keeping the total amount of fuel and air in the system constant, is of the utmost importance in practical gas turbine designs where equivalence ratios in the combustion chamber are highly controlled.

The work presented in this paper aims to provide some detailed in situ soot measurements in a model RQL combustor, focusing on the effect of dilution air location and velocity. This is accomplished by building on previous ex situ experiments, numerical investigations, and preliminary in situ experiments reported in Tracy et al. (2018), Giusti et al. (2018), El Helou (2019) performed on the same RQL burner presented here. Exhaust measurements revealed that both mean particle size and mean particle number drop as dilution air is introduced, and that both these values vary as dilution air location and velocity is changed (Tracy et al. 2018). Numerical results highlighted the importance of local mixing, residence times, and equivalence ratios on reducing soot mass fractions in the RQL at different operating conditions. The goal here is to understand better how the quenching section of the RQL burner affects the flame front and soot formation and oxidation by systematically varying the amount and location of dilution air and investigating their effects through a series of optical and laser diagnostics. This variation of jet location and flow split will extend the understanding presently available on the effect of dilution on soot levels reported in Stöhr et al. (2019), Geigle et al. (2011, 2013, 2015a, b, 2017). These results will also serve to validate numerical investigations such as those presented in Giusti et al. (2018).

## 2 Experimental Setup

A description of the burner used and the main experimental techniques implemented are described in the following subsections.

## 2.1 Burner Setup

Experiments were conducted on an 11 kW non-premixed ethylene–air burner that is bluff-body, swirl-stabilized, and operates at atmospheric conditions. A schematic of the burner can be found in Fig. 1, and is identical to the one used in Tracy et al. (2018), Giusti et al. (2018), El Helou (2019). Gaseous fuel is injected along the axis of the burner through a straight circular channel 4 mm in diameter that passes through the centre of the bluff body. Air is fed from a plenum at room temperature and the primary air passes through a guidevane system referred to as a swirler. The swirler consists of six vanes that rotate the flow clockwise if viewed from downstream. The swirling flow exits through an annulus bounded by the 37 mm outer diameter ( $D_o$ ) of the nozzle and the 25 mm centrally-located conical bluff body. Additional dilution air at room temperature can be injected through four dilution jets positioned downstream of the burner inlet. Each jet, with a diameter of 4 mm, is located at a corner of the square burner, and is constructed so that its axial location, and the amount of air fed through it can be systematically varied. The burner is enclosed by four 3 mm thick quartz plates, 150 mm in height and 97 mm  $\times$  97 mm in cross sectional area. An exhaust hood is placed at the top of the confinement with a square opening of 35 mm  $\times$  35 mm that allows the release of exhaust product gases to the surroundings.

The experiments conducted for the present study build on past work done in El Helou (2019), and look at the effect of dilution air by varying both the axial location of the dilution jets, and the amount of air passing through them. This was accomplished by keeping the total amount of air supplied ( $Q_{total,a}$ ) constant, but varying the split between the air flowing through the primary combustion air inlet ( $Q_{c,a}$ ) and the dilution jets ( $Q_{d,a}$ ). The amount of ethylene ( $Q_f$ ) remained constant at 11.3 SLPM, and  $Q_{total,a}$  remained constant at 600 SLPM for all flames studied. Therefore, the global equivalence ratio ( $\phi_g$ ) remained constant throughout the experiments. Table 1 summarizes the different operating conditions. The Base Case has no dilution. Six other cases were considered at two different ratios of primary to dilution air (80:20 and 60:40), and at three

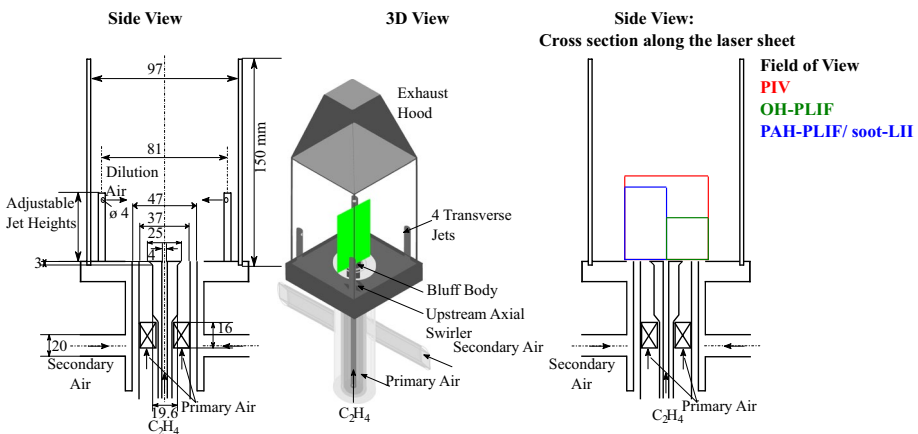


**Fig. 1** Schematics of the side view of the RQL burner with dilution jets (left), 3D view (middle) with the laser sheet passing through the centre of the RQL burner, and cross section of the RQL burner along the laser sheets for the various diagnostics (right)

**Table 1** Tested flame parameters in the burner, with the dilution air velocity reported per jet. Where  $U$  represents velocity,  $Re$  is Reynolds number,  $H_j$  is the height of the dilution jets, and  $\Phi_c$  is the equivalence ratio based on the fuel and primary air alone

Cases	$U_f$ (m/s)	$U_{c,a}$ (m/s)	$U_{d,a}$ (m/s)	$Re$	$H_j$ (mm)	$\Phi_c$	$\Phi_g$
Base	15.0	15.8	0	28,430	0	0.30	0.30
1	15.0	12.7	40	22,850	27	0.37	0.30
2	15.0	9.64	76	17,350	27	0.48	0.30
3	15.0	12.7	40	22,850	47	0.37	0.30
4	15.0	9.64	76	17,350	47	0.48	0.30
5	15.0	12.7	40	22,850	67	0.37	0.30
6	15.0	9.64	76	17,350	67	0.48	0.30

locations of the dilution jets (27, 47, and 67 mm). Alicat mass flow controllers were used to control the flows with a measurement accuracy of  $\pm 0.8\%$  (of the set value) and a full-scale accuracy of  $\pm 0.2\%$ .

## 2.2 High-Speed PIV

Cold flow velocity measurements were obtained for the Base Case, Case 3, and Case 4 in order to investigate the change in the flow as dilution was varied. Although only cold flow (i.e. no fuel flow) was studied, the results can be used for preliminary understanding of the reacting flow. The PIV measurements were performed using a Quantronix Darwin-Duo solid-state diode-pump (SSDP) Nd:YLF dual oscillator/single head laser. After internal frequency conversion, this laser produced radiation near 527 nm at a repetition rate of 2.5 kHz, with a pulse duration of 120 ns, and a temporal separation of 12  $\mu$ s between the independent pulses. The emitted beam then passes through sheet forming optics to expand it into a sheet and align it with the centre of the burner. The final dimensions of the laser sheet formed are 60 mm (tall)  $\times$  0.5 mm (thick). Both the primary and dilution air flows were seeded and the seeding particles used to scatter the light generated by the laser pulses were  $Al_2O_3$  particles 0.3  $\mu$ m in diameter. The small size of the particles used is necessary to ensure that they follow all turbulent fluctuations. The laser power was 27 W, equivalent to 8 mJ/pulse after accounting for the losses in the optics.

1000 image pairs were captured at a rate of 5 kHz using a Photron SA1.1 monochrome high speed CMOS camera operated in a frame-straddling configuration at the maximum camera resolution of 1024  $\times$  1024 pixels. A Nikon 105-mm f/2.8 lens and a 527  $\pm$  20 nm narrow bandpass filter were fitted to the camera to capture the seeded flow field. A final field of view (FOV) of 60  $\times$  60 mm<sup>2</sup> was used for the PIV measurements that gave a projected pixel size of 0.063 mm at the sensor area of 1024  $\times$  1024 pixels. From the raw particle images an average background was subtracted, then the commercial Davis 8 software was used to process the corrected PIV data. In the PIV algorithm, a multi-pass cross-correlation based vector evaluation algorithm was used, with the interrogation window size decreasing from 24  $\times$  24 to 12  $\times$  12 pixels with a 50% overlap to determine the displacement of the particles at many localized positions within the

images. This resulted in a velocity interrogation region of 0.76 mm and vector spacing of 0.38 mm.

### 2.3 Flame Photographs and OH\* Chemiluminescence

A Nikon DX AF-S camera equipped with an 18–55 mm lens with no added filter was used to capture photographs of the flame. Both long (1/10 s) and short (1/2000 s) exposure images were captured with apertures  $f/5$  and  $f/32$ , respectively, to yield sufficient levels of light. This provided approximations to an instantaneous and a time-averaged photograph of the flame. The camera settings and ISO sensitivity were kept constant for all the cases for comparability while ensuring no image saturation occurs with the higher intensity flames (Base Case) during longer exposure times. For each condition, OH\* chemiluminescence images were captured as they provide qualitative information into the heat release rate. The chemiluminescence images were taken with a CMOS camera system (LaVision IRO high-speed two stage intensifier and Photron SA1.1 monochrome high-speed CMOS camera) fitted with a UV lens (Cerco 2178) and a  $300 \pm 10$  nm bandpass filter (Andover). This filter was chosen as OH\* radicals are known to strongly emit around the 310 nm range, and a narrow Full width at half maximum (FWHM) of 10 nm helps in reducing interferences from other radicals. The camera gate was varied between 100 and  $180 \mu\text{s}$  in order to improve the signal to noise ratio. Therefore, the captured images provide a qualitative comparison of the distribution of the OH\* signal, however the intensity relative to one another cannot be compared because of the varying exposure times. The RQL burner produces a flame that is mostly below the location of the jets and at radii not too close to the walls, which makes the flame approximately axisymmetric. Therefore, an inverse Abel transform can be applied on the line of sight images that give a 2D projection of the OH\* onto a plane so as to get a better approximation to the location of the average reaction zones.

### 2.4 High-Speed OH-PLIF

High-Speed OH-PLIF experiments were performed using a 14 W pulsed JDSU Q-series Nd:YAG laser that emits a 532 nm beam for a length of 18 ns at a 5 kHz repetition rate that is directed through mirrors into the Sirah Credo 2400 high-speed dye laser. The dye laser was operated with Rhodamine 6G (R6G) dye to produce a beam at 566 nm, which was frequency-doubled with an internal BBO crystal to produce a beam near 283 nm. Specifically, the output from the dye laser was tuned to excite the  $Q_1(6)$  transition in the  $A^2\Sigma^+ - X^2\Pi(v' = 1, v'' = 0)$  band of OH. The laser beam is then directed through sheet forming optics that form a 28 mm (tall)  $\times$  0.12 mm (thick) laser sheet that is aligned with the centre of the burner. The final beam has an average power of 300 mW at 5 kHz equivalent to  $50 \mu\text{J}/\text{pulse}$  after accounting for the losses through the optics. The thickness is estimated through a scanning knife-edge technique Wang and Clemens (2004) performed using a blade and a power meter. The laser sheet produced does not have a uniform intensity in the vertical direction. Corrections were performed on an average basis using a dye cell with R6G, revealing a Gaussian distribution within the laser sheet over the range of 0.1–1, which were applied on the OH-PLIF images captured.

5000 images were captured using an identical camera setup to that of the chemiluminescence experiments, fitted with a UV lens (Cerco) and a  $310 \pm 10$  nm narrow bandpass filter (Andover). The filter with a narrow full width at half maximum (FWHM) of 10 nm proved

ideal in rejecting interferences from soot incandescence. The laser sheet was aligned with the centre of the burner and its height allowed for a 28 mm × 28 mm FOV with a projected pixel size of 20 μm as can be seen in Fig. 1. Finally, the camera settings were set to a gate of 300 ns and a gain of 60, while the camera delay was adjusted to ensure the camera gate lines up with the laser pulse.

## 2.5 Low Speed PAH-PLIF and LII of soot

Low-speed PLIF and LII techniques have been widely used for the imaging of polycyclic aromatic hydrocarbons (PAHs), and soot respectively, and the setups used here are identical to the ones described in El Helou (2019). For both measurements of PAH-PLIF and LII of soot, a pulsed Continuum Surelite II Nd:YAG laser at repetition rates of 10 Hz and pulse duration of 9 ns was used. Excitation wavelengths for the PLIF and LII measurements of 266 nm (the fourth harmonic), and 532 nm (the second harmonic), respectively were used. The choice of excitation wavelength is very important in LII measurements. A wavelength of 532 nm was used here to excite soot particles as it fulfills the critical Rayleigh absorption criterion of  $\pi D/\lambda \ll 1$  (Singh et al. 2016), where  $D$  is the diameter of the soot particles and  $\lambda$  is the excitation wavelength. Note that LII is not expected to give signal from particles outside the range of 5–100 nm as smaller particles behave like molecules and do not incandesce, while larger particles do not satisfy the Rayleigh criterion (D'Anna 2009a; Singh et al. 2016). The same sheet forming optics were used to form the laser sheet from the emitted laser beam for both LII and PAH experiments. The final laser sheet formed is aligned with the centre of the burner, and has dimensions of 52 mm (tall) × 0.18 mm (thick).

An important variable that was optimized was the power of the laser to improve the quality of the PLIF and LII images. For PAH measurements, the laser fluence was kept low to eliminate soot incandescence and interference from LII signals (Köhler et al. 2011; Shaddix and Smyth 1996; Singh et al. 2016). After taking into account the losses from the optics the final laser power used was 20 mW equivalent to 19 mJ/cm<sup>2</sup>. For the LII measurements, a high enough power was selected to ensure operation within the plateau regime, where soot particles incandescence is independent of laser fluence. This laser fluence has been shown in previous work to be greater than 0.5 J/cm<sup>2</sup> (Köhler et al. 2011; Shaddix and Smyth 1996; Singh et al. 2016). After taking into account the losses from the optics the final laser power used was 2 W equivalent to 1.9 J/cm<sup>2</sup>. In the plateau regime the incandescence of soot particles is independent of laser power; therefore, there is no need to correct for fluctuations in laser power either spatially or temporally. Shot-to-shot corrections were not needed as a well-expanded laser sheet that was relatively uniform was used such that saturation was achieved at each vertical location within the sheet. Laser sheet corrections using an identical technique to the OH-PLIF corrections were performed on the PAH-PLIF images, as the laser sheet showed a variation in intensity in the vertical direction. Corrections revealed a Gaussian distribution within the laser sheet over the range of 0.9–1 which were applied to the PAH images.

800 instantaneous images were recorded at 10 Hz sampling rate with a LA VISION NanoStar2 CMOS camera. The camera was equipped with a 100-mm f/2 Zeiss lens and a 430 ± 25 nm Semrock BP filter. The choice of this filter minimizes PAH interference during LII experiments, as they fluoresce at wavelengths greater than the 532 nm excitation. Additionally, at this detection wavelength only larger PAHs can be detected during PLIF experiments, as emission wavelengths are highly dependent on the number of aromatic



rings of the PAHs. Using a scanning knife edge technique (Wang and Clemens 2004), the system resolution was measured at  $250\ \mu\text{m}$ . The exposure time was always less than 40 ns to minimize interference from chemiluminescence and to ensure sufficient capture of PLIF and LII signal in all the tested cases. The detected LIF and LII signals vary for the studied cases; therefore, the settings were chosen by testing the cases with both the highest and lowest signals to ensure that the chosen gain and gate were adequate for the full range of experiments. The laser sheet was aligned with the centre of the burner and a FOV of  $52\ \text{mm} \times 60\ \text{mm}$  was attained at a projected pixel size of  $0.095\ \text{mm}$  as can be seen in Fig. 1.

The delay between the laser pulse and the camera is an important parameter to control. This delay was eliminated when imaging PAHs, as LIF signals decay within approximately 10 ns; therefore, to capture the fluoresces within a 40 ns gate, the gate and the arrival of the laser were overlapped. During LII imaging, LII signals persist over approximately 100 ns, and a 60 ns delay was applied to ensure that the PAHs have reacted and nucleated to form soot particles. This delay is sufficient to avoid LIF generated, short lived blue shifted contributions, as they have a lifetime of approximately 10 ns (Singh et al. 2016).  $\text{C}_2$  sublimation off the surface of the soot particles emit in the range of 420–650 nm, and are an additional source of interference, but they have a short lifetime of 5 ns (Singh et al. 2016); therefore, the chosen delay is enough to minimize this interference. Soot particle cooling times vary widely as they are dependent on the ratio of the soot surface area to volume; thus smaller particles cool down faster and the delay used for all the cases favours the slower cooling larger particles (Singh et al. 2016).

Similar image processing schemes were applied to both the high-speed OH-PLIF images and the low speed LII and PAH-PLIF images. First, background fields (i.e. those resulting from dark current in the camera, flame chemiluminescence, and unrejected elastically scattered laser light) were subtracted. Subsequently, in the case of the PAH-PLIF and OH-PLIF images, an average laser sheet correction was applied. Finally, to enhance the signal to noise ratios, a median filter with a kernel size of  $3 \times 3\ \text{pixel}^2$  was applied to all image types.

### 3 Results

The following section details the key findings from operating the RQL with and without dilution air. The change in time averaged velocity fields, and time averaged OH, PAH and soot distributions are compared to identify the main differences in the various flames.

#### 3.1 Cold Flow PIV

Cold flow velocity data with and without dilution air for the Base Case and Cases 3 and 4 are shown in Fig. 2 for qualitative understanding of the flow structure and the extent of the recirculation zone with the two injection strategies. The Base Case velocity field is characteristic of a swirled non-premixed turbulent flow with the high-velocity inlet flow defining the inner and outer shear layers (ISL and OSL respectively), as well as both a central and outer recirculation zones (CRZ and ORZ respectively). The CRZ extends beyond 60 mm and is present throughout the field of view. Once dilution air is introduced at 20% in Case 3 the high velocity inlet flow is still evident, but the CRZ narrows as it is bounded by the radially injected dilution air. The edge of the CRZ is now within the field of view and terminates at 60 mm. This additional dilution air increases the velocities in the CRZ

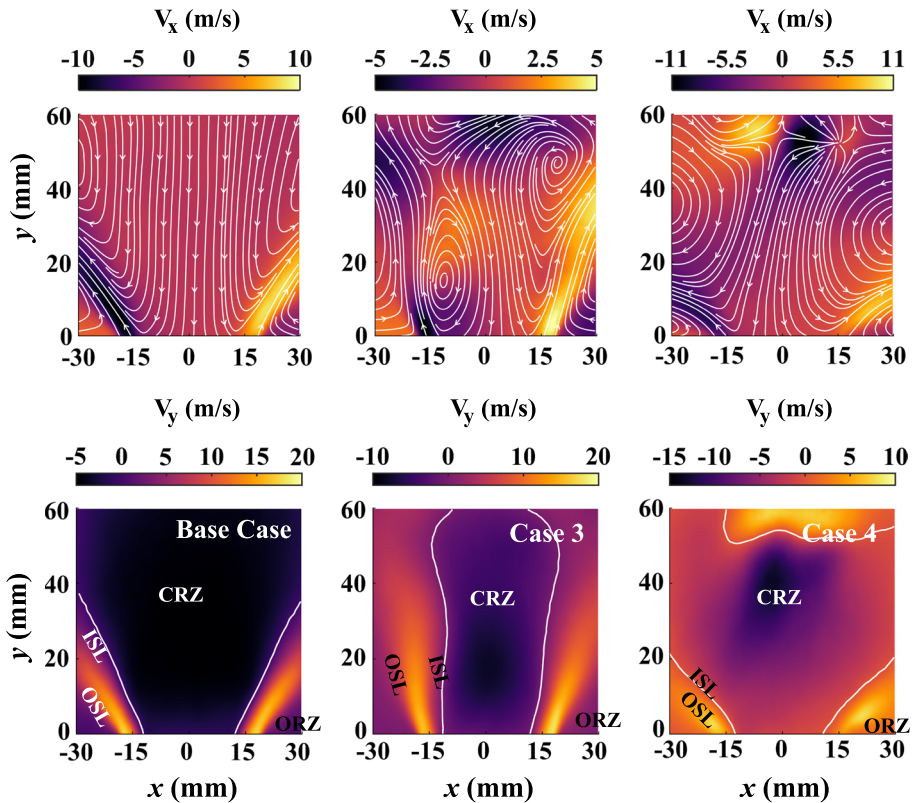


**Fig. 2** Top row: time-averaged cold flow contour plots of the radial velocity fields ( $V_x$ ) for the Base Case (left), Case 3 (middle), and Case 4 (right). The velocity vectors represent the axial and radial velocity components. Bottom row: time-averaged cold flow contour plots of the axial velocity fields ( $V_y$ ) for the Base Case (left), Case 3 (middle), and Case 4 (right) superimposed with the solid white line representing the  $V_y = 0$  m/s contour. The central recirculation zone, internal shear layer, outer shear layer and outer recirculation zone are labeled as CRZ, ISL, OSL and ORZ respectively. Axis of burner is at  $x = 0$

relative to the Base Case as can be seen in the  $V_y$  contours of Fig. 2. When dilution air is increased to 40% in Case 4, the high momentum dilution air creates a clear stagnation point at 50 mm and splits, part of it recirculating to the root of the flame, while the rest flows upward similarly to Case 3. However, the higher dilution air momentum in this case creates another location of high velocity at 50 mm, comparable to the velocities of the inlet flow. The higher velocities and added flow of air in the CRZ as well as the alteration to the size and shape of the CRZ in Cases 3 and 4 compared to the Base Case all have an effect on the formation and oxidation of soot particles as will be discussed in the following sections.

### 3.2 Flame Photographs and OH\* Chemiluminescence

Flame photographs of the Base Case, and Cases 1–6 are displayed in Figs. 3 and 4. Two changes to the flame are visibly noticeable as dilution air is introduced, increased, and as the dilution jet locations are varied. At base conditions the flame encompasses 80 mm

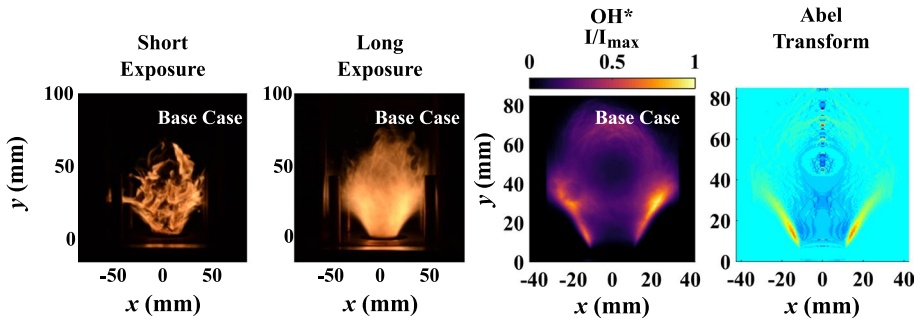


**Fig. 3** Left two images: flame photographs of the Base Case. These images were taken with a short exposure time of 1/2000 s (left of the two photographs), and long exposure time 1/10 s (right of the two photographs) to represent instantaneous and average images respectively. Right two images: averaged OH\* chemiluminescence image normalized by its maximum signal (left of the two images), and its Abel transform (right of the two images) of the Base Case. Axis of burner is at  $x = 0$

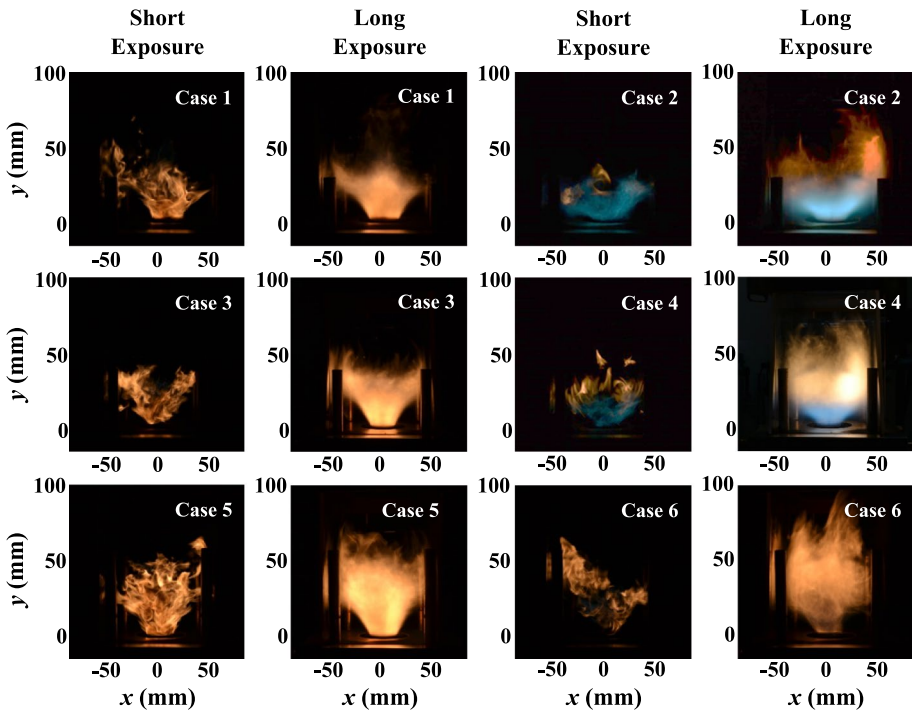


**Fig. 4** Flame photographs of Cases 1–6 taken with a short exposure time of 1/2000 s (first and third column), and long exposure time 1/10 s (second and fourth column) to represent instantaneous and average images respectively. Axis of burner is at  $x = 0$

(54%) of the burner length, and is yellow in color indicative of a sooting flame. Once dilution air is injected at an 80:20 split, the flame becomes visibly shorter at less than 50 mm (35%) of the burner length for Cases 1 and 3 at jet heights of 27 mm and 47 mm

respectively. While in Case 5 at a jet height of 67 mm, the flame is longer than in Case 3 and covers around 70 mm (47%) of the burner length. In Cases 1, 3, and 5 the color of the flame remains yellow and sooting. When the split increases to 60:40 for Cases 2 and 4 at jet heights of 27 mm and 47 mm respectively, the flame is once again shorter at approximately 65 mm (43%). The most visible change is the change in color of the lower half of the flame from the luminescent yellow/orange associated with soot, to the blue, indicative of a cleaner less sooting flame, while the flame maintains a yellow color farther downstream from the burner inlet. While in Case 6, at a jet height of 67 mm, the flame is once again longer at 80 mm (54%), and the color remains yellow. These photographs are a first indication that the location of the dilution jets and the amount of air radially injected through them, affect drastically the length and color of the flame.

Average  $\text{OH}^*$  chemiluminescence images, and their equivalent inverse Abel transforms for the Base Case and Cases 1–6 are in Figs. 3 and 5 respectively. For the Base Case, the average length of the reaction zone is 75 mm. The signal peaks along the ISL and is stabilized on the edge of the bluff body. This is in agreement with other non-premixed, swirling flames (Cavaliere et al. 2013). There is no signal in the ORZ, and the signal decreases in the CRZ. In Cases 1, 3, and 5, where the air split is 80:20, the length of the reaction zone is shortened to 45 mm, 50 mm, and 70 mm respectively. These Cases maintain similar trends

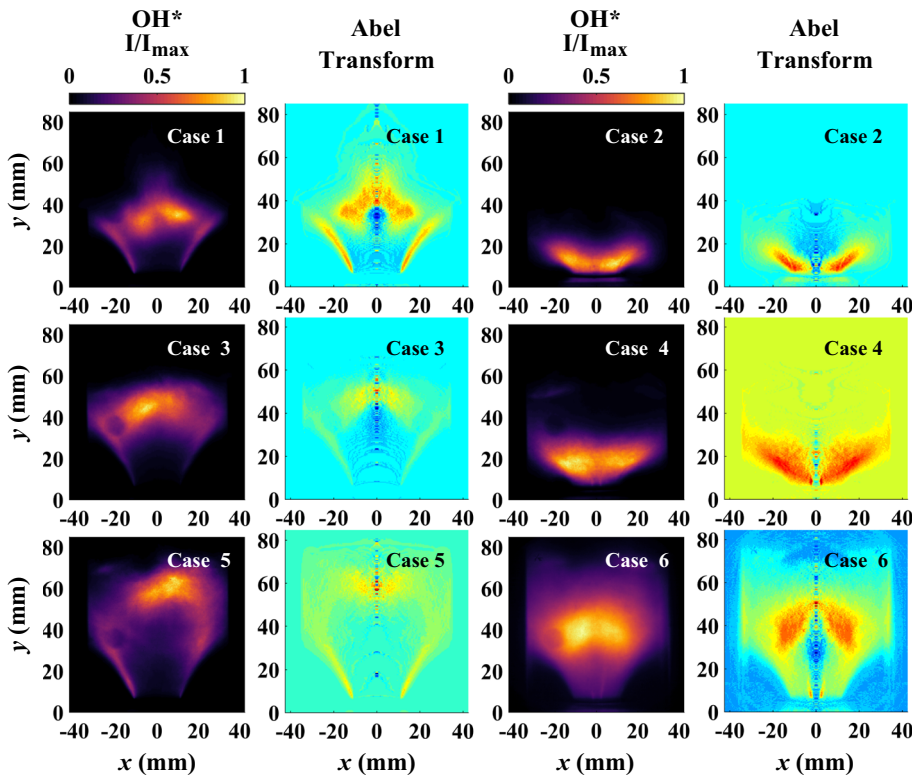


**Fig. 5** Averaged  $\text{OH}^*$  chemiluminescence images (first and third columns), and their Abel transforms (second and fourth columns) of Cases 1–6. The  $\text{OH}^*$  chemiluminescence images are normalized by the maximum signal in each case. Axis of burner is at  $x = 0$

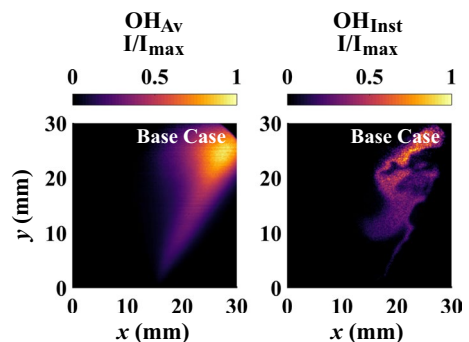
to the Base Case in certain aspects. There is no signal in the ORZ nor along the base of the burner. There is also a hollowing out of the signal at the lower end of the CRZ. However, the peak OH\* signal is no longer along the ISL but has shifted to the centre of the reaction zone along the top of the CRZ in all three cases. The maximum heat release is now axially between 25–35 mm, 35–45 mm, and 55–65 mm for Cases 1, 3 and 5 respectively. This maximum heat release location coincides with the location of the dilution jets. In Cases 2 and 4 where the air split is now 60:40 with the dilution air injected at heights of 27 mm and 47 mm respectively there are significant changes to the heat release compared to the Base Case. There is no signal in the ORZ, additionally there is no signal downstream of the dilution air injection point. The region of heat release is confined between the burner inlet and the radial dilution jets. The heat release has a homogeneous spread within the CRZ and the reaction zone is stabilized on the bluff body. In Case 6, similar attributes are shared with Cases 2 and 4; however, the spread of heat release extends to 65 mm downstream of the burner inlet, with the signal spreading throughout the CRZ without the hollowing out evident in Case 5. Additionally, the signal is at its maximum between  $y = 35\text{--}55$  mm. The signal is not as homogeneous as Cases 2 and 4 because of the larger distance between the burner inlet and the location of the dilution jets. These results reveal a fundamental change in the flame shape and location with dilution, which implies a potentially large difference in the residence time and strain rate of the soot-producing mixture fractions, and hence a fundamental change in the soot produced.

### 3.3 High-Speed OH-PLIF

The average and instantaneous OH-PLIF images of the Base Case can be found in Fig. 6. The flame front is stabilized on the edge of the bluff body (at  $x = 12.5$  mm), although occasional lift-off may occur. The OH distribution is narrow and approximately aligned with the annular shear layer. The average OH peaks at around  $x = 20$  mm. On either side of the shear layer at locations corresponding to the central and outer recirculation zones there is no OH signal present. These observations in the Base Case with an ethylene flame are consistent with the CH<sub>4</sub> flame in the same burner (with no dilution) described in Cavaliere et al. (2013).

Averaged and instantaneous OH-PLIF images of Cases 1–6 can be found in Fig. 7. Once 20% dilution air is introduced at a height of 27 mm (Case 1) the OH signal remains concentrated in the shear layer similarly to the Base Case. However, the OH distribution is wider than that of the Base Case, and is closer to the axis as a result of dilution air injected

**Fig. 6** High speed averaged OH-PLIF images (left), and high speed instantaneous OH-PLIF images (right) for the Base Case. The field of view is shifted for these measurements and shows one half of the flame front. Axis of burner is at  $x = 0$



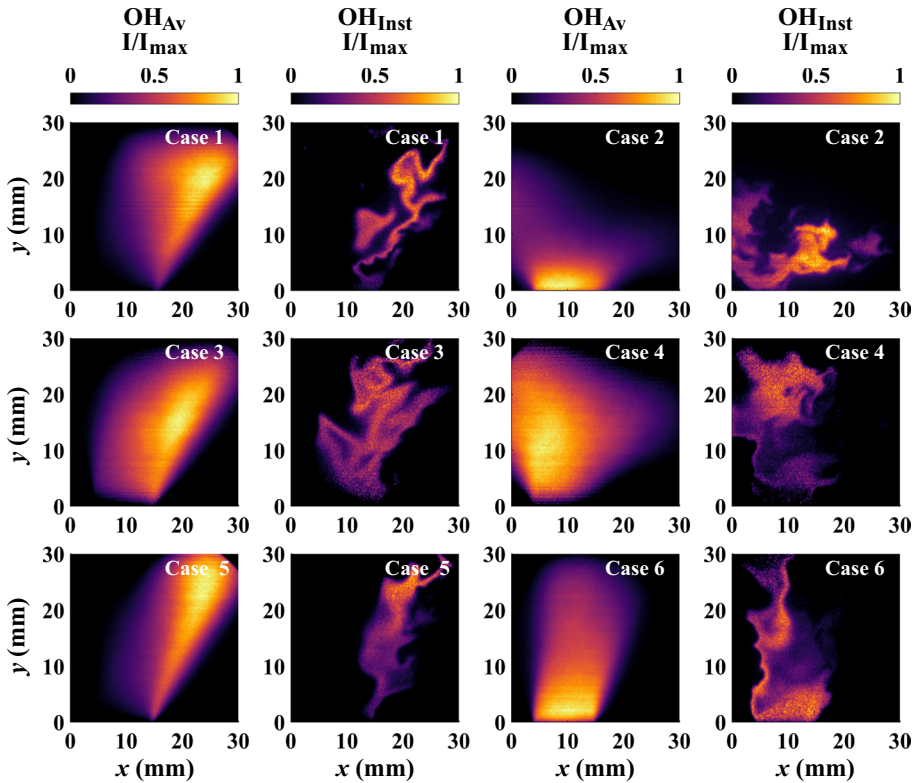


**Fig. 7** High-speed averaged OH-PLIF images (first and third column), and high-speed instantaneous OH-PLIF images (second and fourth column) for Cases 1–6. The field of view is shifted for these measurements and shows one half of the flame front. Axis of burner is at  $x = 0$

radially at a location that is close to the burner inlet. The high intensity OH signal is more uniformly distributed along the ISL rather than concentrated farther downstream as in the Base Case. As the dilution jets are moved to the second position at a height of 47 mm and 20% dilution in Case 3 a similar spread of OH is detected. As dilution air increases to 40% (Case 2 with jets at 27 mm) the OH distribution no longer bears any resemblance to the Base Case. The distribution is wider, spanning virtually the whole width of the CRZ, with the dark region corresponding to the fuel jet severely reduced along the axis, and the peak signal shifting to the root of the flame. As the momentum of the dilution jets doubles from Case 1, the jets penetrate the CRZ, turbulent mixing increases, and the flame shortens, as has also been seen in the flame photographs and OH\* chemiluminescence images of Figs. 4 and 5.

As the location of the dilution jets is moved farther downstream to 47 mm at 40% dilution (Case 4) the OH distribution is wider with the central dark region reduced. Additionally, the signal spreads farther downstream compared to Case 2 due to the larger distance between the dilution jets and burner inlet (about two bluff body diameters). Moving the dilution jets to the final location of 67 mm, at 20% dilution (case 5) the OH distribution narrows and is the most similar in shape to the Base Case; in this downstream location the jets seem to have little influence on the CRZ and the fuel distribution. As for 40% dilution

(case 6) the OH distribution is more widespread, somewhere in between the shapes seen in Cases 1, 3 and 5 and Cases 2 and 4. As with the Base Case, the small field of view does not fully capture the OH distribution in Cases 5 and 6.

Looking at Cases 1, 3 and 5 together, the flame seems stabilised on the edge of the bluff body, while looking at Cases 2, 4 and 6 the flame is stabilised very close to the bluff body rather than on its edge. This is due to the higher momentum dilution air that reduces the fuel jet penetration length, and increases turbulent mixing between the fuel and the air, while radially constricting the recirculation zone so as to cause this shift towards the CRZ. As the dilution air is introduced and increased the spread of OH changes from what is expected in turbulent non-premixed flames to a distribution similar to those seen in turbulent premixed flames (Cavaliere et al. 2013). This reveals that the dilution air alters dramatically the mixture fraction distribution, especially when injected close to the bluff body and at high speeds (Cases 2 and 4 with dilution velocities ten times that of the primary air).

### 3.4 PAH-PLIF and LII of Soot

The OH\* chemiluminescence images revealed that the flames formed in the RQL burner are axisymmetric; therefore, all PLIF and LII experiments were performed on one half of the burner. Figure 8 displays the average and instantaneous soot-LII and PAH-PLIF results for the Base Case. For the Base Case, both the LII and LIF signals are present throughout the field of view. The LII signal is concentrated within the CRZ while the LIF signal is concentrated along the axis of the burner (i.e. along the fuel jet), with the signal weakening farther away from the axis. The PAH is not evident at the early parts of the fuel jet (up to about  $x = 10$  mm) along the axis, presumably because the mixture fraction is too rich there for PAHs to form. From the instantaneous images it is clear that soot forms in filaments, while PAHs are more continuously distributed. The presence of soot within the CRZ is in agreement with previous works that have shown soot formation favours regions of low velocity and long residence times compatible with the slow chemistry associated with soot formation (Stöhr et al. 2019; Narayanaswamy and Clemens 2013).

Average and instantaneous LII and PLIF images of Cases 1-6 are shown in Fig. 9. In the Base Case, the majority of the PAH-PLIF and LII detected signal is 50% or greater than the

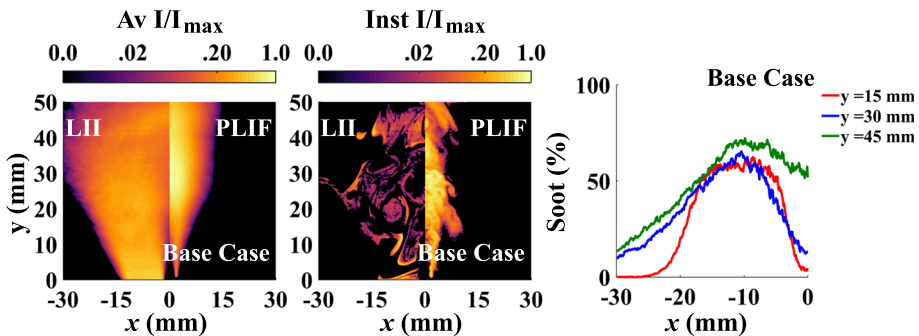


**Fig. 8** Average (left) and instantaneous (middle) LII and PAH-PLIF image pairs of the Base Case. Within each image: averaged/instantaneous LII image (left half), averaged/instantaneous PLIF image (right half). Average images normalized by the maximum PLIF/LII signal of the Base Case plotted on a logarithmic scale. Axis of burner is at  $x = 0$ . (Right) the probability of soot presence as a function of radial distance at three axial locations for the Base Case

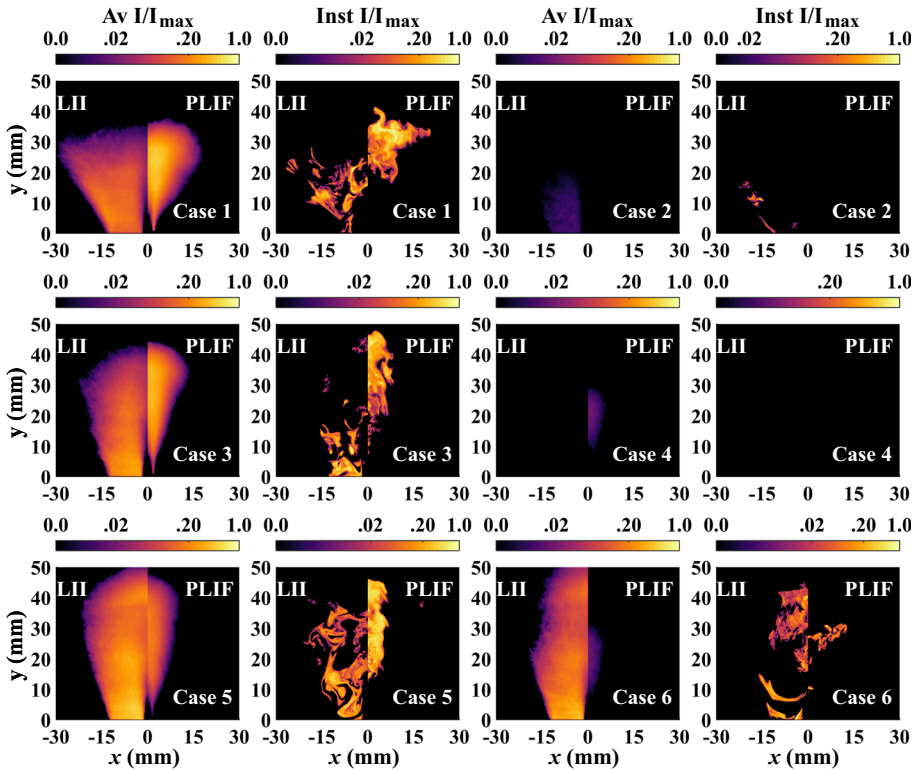


**Fig. 9** Average (first and third column) and instantaneous (second and fourth) LII and PLIF image pairs of Cases 1–6. Within each image: averaged/instantaneous LII image (left half), averaged/instantaneous PLIF image (right half). Average images normalized by the maximum PLIF/LII signal of the Base Case plotted on a logarithmic scale in order to clearly display the influence of dilution level and location. Axis of burner is at  $x = 0$

maximum signal in this Case ( $I_{BC,max}$ ). Once dilution air is introduced at 20% the LII signal drops to 35% or lower than that of  $I_{BC,max}$  for Case 1 at a jet height of 27 mm. The signal rises once again as the dilution jets are moved farther from the burner inlet, and is 65% or lower than  $I_{BC,max}$  for Case 3 at a jet height of 47 mm. At a jet height of 67 mm in Case 5 the LII signal is 150% that of the Base Case in some locations close to the burner inlet. The PAH-PLIF signal behaves in an inverse way and drops in intensity as the dilution jets are placed farther downstream. The signal drops to 65%, 40% and 20% or lower than that of the Base Case for Cases 1, 3 and 5, respectively. It is evident from all three Cases that the PAHs and soot were prevented from propagating beyond 35 mm, 40 mm, and 50 mm for Cases 1, 3 and 5, respectively, terminating at the dilution injection point. Additionally, as the dilution jets' location is moved farther downstream the spread of LII and LIF signal narrows and elongates as the distance between the primary air and fuel, and the dilution air increases.

In Cases 1, 3 and 5 the LII signal is strongest closer to the bluff body and diminishes as the dilution jets are approached. This is evident in the instantaneous images where the majority of the LII filaments form close to the bluff body. The LIF signal in Cases 1, 3 and 5 is concentrated along the burner axis and diminishes radially outward compared to the



LIF signal in the Base Case. In all three Cases the LIF signal is lower than the Base Case. In Cases 3 and 5 the LIF signals reduce as less PAHs are formed compared to Case 1. PAH detection is highly dependent on the filter used; in these experiments the detection wavelength was approximately 430 nm which is optimal for 4 ring PAHs such as pyrene (Singh and Sung 2016). What these results reveal is that as dilution air is moved farther away from the primary combustion zone less pyrenes are formed. However, there is no further information on the amount of smaller or larger ringed PAHs present. The formation of PAHs is highly dependent on many parameters such as local flame conditions, and temperature (Singh and Sung 2016). As the location of dilution air and the amount injected is varied, the mixture fraction distribution changes, the velocity field (mean, turbulence, strain rates) also changes, which is likely to have an effect on local flame temperatures, and thus affects the PAHs formed (Singh and Sung 2016).

Once dilution air is increased to 40%, LII signal is no longer evident in Cases 2 and 4 at less than 2% of  $I_{BC,max}$  at a jet height of 27 mm and less than 1% of  $I_{BC,max}$  at a jet height of 47 mm. The injection of dilution air leads to increased turbulent mixing as the jets meet at the axis of the burner and circulate upstream: opposing the fuel jet and reducing its penetration length, increasing the recirculation of hot combustion products, widening the spread of OH and increasing velocities in the CRZ. The injected dilution air splits and either flows to the exhaust or to the root of the flame as was seen in Fig. 2 which leads to a further oxidation of larger soot particles already formed. At a jet height of 67 mm in Case 6 the LII signal is still greater than that of the Base Case at 123% in some locations close to the burner inlet, but less than the signal in Case 5. The LIF signal is not distinguishable for Case 2; however, the signal remains at less than 2% of  $I_{BC,max}$  as the dilution jets are moved farther downstream in Cases 4 and 6. It is evident from Cases 2 and 4 that lower concentrations of PAHs and soot formed compared to both the lower dilution cases (Cases 1 and 3) and the Base Case. For Case 6, lower concentrations of PAHs formed as the dilution air was increased similarly to Cases 2 and 4. However, larger soot particles still formed unlike the other high dilution Cases, similarly to Case 5 but at lower concentrations. In Case 6, the increased dilution air is counteracted by the larger distance between the burner inlet and the dilution jets reducing their influence in the primary reaction zone. The reduced primary air and reduced effectiveness of the dilution air in Cases 5 and 6 leads to a richer primary combustion zone and thus a higher concentration of large soot particles formed at the root of the flame up until  $y = 10$  mm within the burner compared to the Base Case. Soot concentrations drop steadily past 10 mm as the dilution jets are approached. The concentration of soot particles formed in Case 6 is lower than that of Case 5 due to the higher momentum dilution air that increases the oxidation of the formed soot particles. These six Cases highlight the importance of both the dilution jet location, and the amount of dilution air injected at reducing soot formation and increasing soot oxidation.

To understand further the effectiveness of the different air dilution strategies at reducing soot production, the probability of soot presence, i.e. the probability of LII signal being greater than 0, was calculated and is plotted in Fig. 8 for the Base Case, and in Fig. 10 for Cases 1–6. In the Base Case, all three axial profiles reveal that soot detection rises steadily from the axis outwards and peaks past  $x = 5$  mm where it is detected more than 50% of the time. For all three profiles this percentage drops to below 50% of the time past  $x = 20$  mm from the centre of the burner, and at a  $y = 15$  mm in particular no soot forms in the ORZ. In Cases 1, 3 and 5, for the  $y = 15$  mm profile, soot presence rises steadily away from the axis before peaking at  $x = 5$  mm. In the range  $5 < x < 20$  mm, soot forms 25%

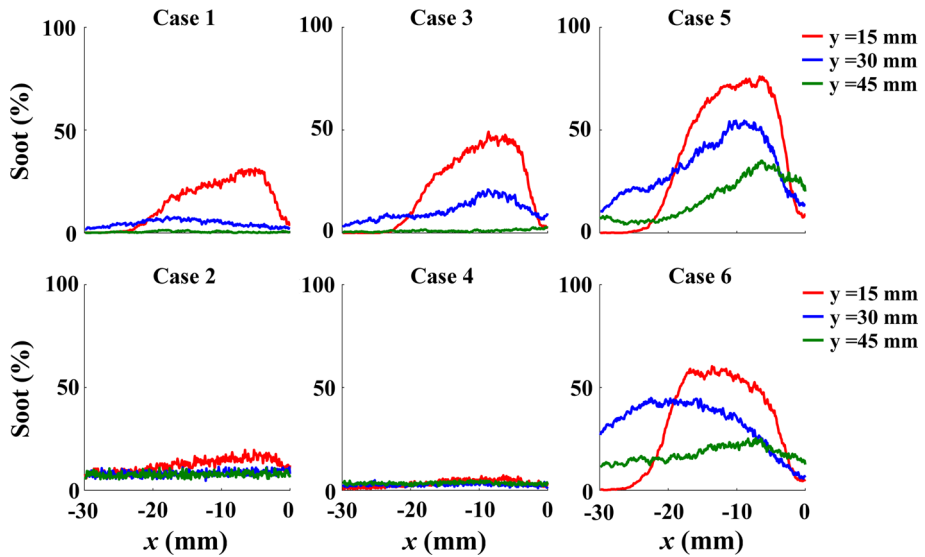


**Fig. 10** The probability of soot presence as a function of radial distance at three axial locations for Cases 1–6

of the time, less than 50% and around 75% of the time for Cases 1, 3, and 5 respectively. Past  $x = 20$  mm soot particles no longer form as the ORZ is approached. At a  $y = 30$  mm, the probability of soot presence is homogeneously low and drops below 5% and 10% for Cases 1 and 3, respectively, as soot intermittency increases. At  $y = 45$  mm virtually no soot is distinguishable for both Cases. Soot probability is still higher for Case 3 over Case 1 up until the  $y = 30$  mm profile due to the farther placed dilution jets. However, in Case 5 the dilution jets are placed farther downstream, and thus are no longer as effective at mitigating soot formation. Past  $y = 15$  mm, soot forms 50% of the time at the  $y = 30$  mm profile, and then drops to 25% as the jets are approached at  $y = 45$  mm. Once dilution air is increased to 40%, soot intermittency increases as soot is detected 10% and 5% of the time in Cases 2 and 4 respectively for all three profiles. In Case 6 the added effect of higher air dilution momentum is counteracted by the increased distance between the burner inlet and the dilution jets. Soot forms more consistently along the three profiles compared to Cases 2 and 4, with a distribution similar to Case 5 with 20% dilution air. These distributions for Cases 5 and 6 reiterate that while soot intermittency is similar to the Base Case at the lower profile of  $y = 15$  mm that is no longer the case farther downstream at  $y = 30$  mm and 45 mm as intermittency increases as the dilution jets are approached.

Finally, in Fig. 11 the average distributions of the PAH-LIF, OH-LIF and soot-LII signals are compared qualitatively for all flames. In the Base Case, all three signals increase away from the burner inlet. The PAH signal peaks along the axis of the burner, as it decreases the soot signal peaks within the CRZ and the soot signal drops as the OH signal peaks along the ISL. In Cases 1 and 3 at 20% dilution injected at heights of 27 mm, and 47 mm respectively, similar patterns are evident with a lower and narrower spread of soot signal within the CRZ as the OH signal rises and widens. In Case 5 at 20% dilution injected at a height of 67 mm the signal distributions are the most similar to the Base Case, as the distance between the burner

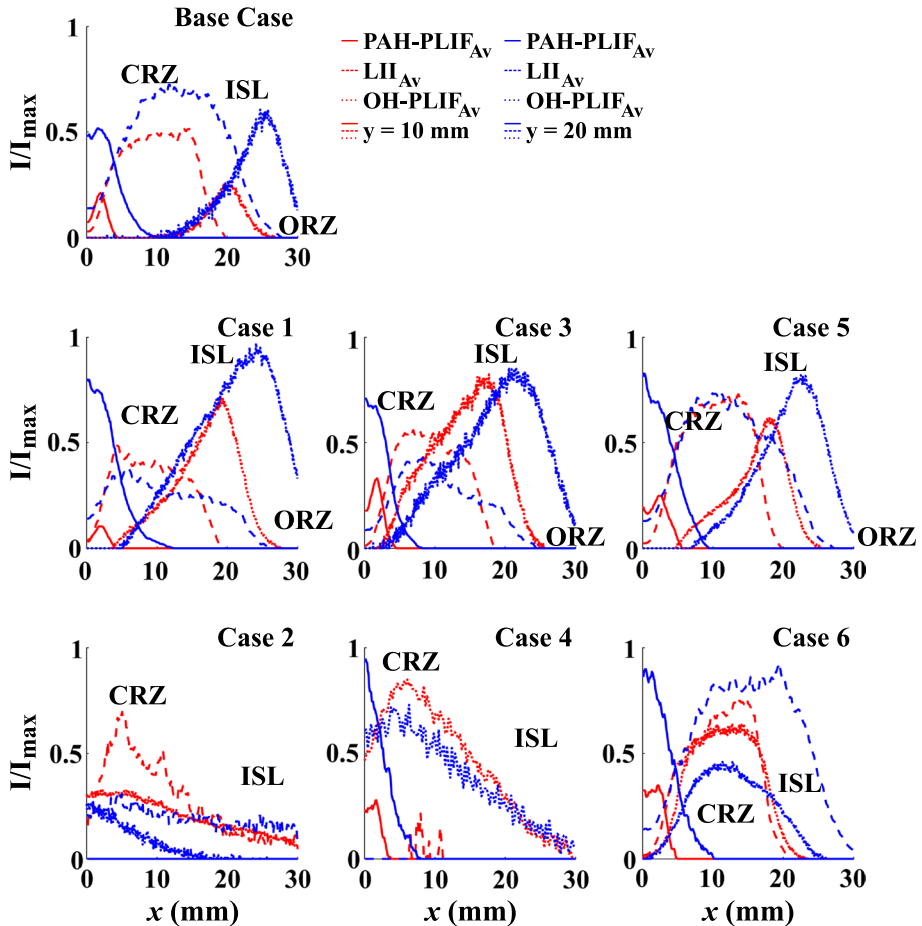


**Fig. 11** Radial distributions of the average OH-LIF, PAH-LIF and LII signals at two axial locations for the Base Case, and Cases 1–6. All signals are normalized by the maximum intensity in each respective Case. The locations of the CRZ, ORZ, and ISL are marked

inlet and the dilution jets increases which reduces their effectiveness. Once the dilution air is increased to 40% at a height of 27 mm and 47 mm in Cases 2 and 4 the OH distribution widens breaching the CRZ with a higher signal in the CRZ compared to the ISL. In Case 2 the OH signal is homogeneously distributed leading to no PAH signal being detected, while some soot is detected at low levels narrowly distributed within the CRZ below the dilution air injection point. In Case 4 the high intensity OH signal within the CRZ in the location where soot peaks leads to negligible soot signals within the CRZ while PAH signals are still detected along the axis where OH signals have not yet peaked. When the dilution jets are positioned at a height of 67 mm and 40% air is injected through them their effect is counteracted by the large distance between the jets and the burner inlet. This leads to the presence of PAH signal along the axis where there is no OH signal. However, the spread of OH changes compared to all other Cases and has a wide spread within the CRZ between  $5 < x < 20$  mm from the centre of the burner. The OH signal decreases away from the burner inlet as the dilution jets are

too far downstream in this Case. This leads to a richer primary combustion zone and a larger detected LII signal within the CRZ at both axial locations.

## 4 Conclusions

A model RQL combustor was investigated with in situ laser diagnostics to understand the changes to the flame front and soot formation as a result of dilution air. OH\* chemiluminescence, high-speed OH-PLIF, and low speed LII of soot and PAH-PLIF were performed as the location and amount of dilution air injected were systematically varied. Results of the OH-PLIF revealed changes to the flame front due to dilution air. The spread of OH widened but remained concentrated along the shear layer when dilution air was introduced at 20% of the total air flow. However, when dilution air was increased the OH regions occupied the whole CRZ width and the peak heat release shifted towards the axis of the burner. PAH-PLIF and LII experiments revealed the change in PAH and soot distributions as dilution air was introduced and increased. The location of the dilution jets relative to the CRZ, where soot is formed, is important for mitigating soot formation and increasing soot oxidation. The dilution air at distances up to two bluff body diameters increases the spread of OH within the CRZ, increases turbulent mixing, reduces the fuel jet penetration length, and reduces residence times thus reducing soot formation and oxidizing larger soot particles formed. Dilution jets at distances farther downstream are less effective at mitigating soot formation and lead to higher soot concentrations in the primary combustion zone compared to the Base Case.

Future work will focus on further optical diagnostics especially to investigate the flow field. These results are necessary for the optimization of burner designs to reduce soot formation, and the development and validation of numerical models aiming to accurately simulate turbulent sooting flames.

**Acknowledgements** The authors would like to acknowledge the Rolls Royce Group and the EPSRC Gas Turbine Aerodynamics CDT for funding this work (EPSRC grant reference: EP/L015943/1).

## Compliance with ethical standards

**Conflict of interest** The authors declare that they have no conflicts of interest.

**Open Access** This article is licensed under a Creative Commons Attribution 4.0 International License, which permits use, sharing, adaptation, distribution and reproduction in any medium or format, as long as you give appropriate credit to the original author(s) and the source, provide a link to the Creative Commons licence, and indicate if changes were made. The images or other third party material in this article are included in the article's Creative Commons licence, unless indicated otherwise in a credit line to the material. If material is not included in the article's Creative Commons licence and your intended use is not permitted by statutory regulation or exceeds the permitted use, you will need to obtain permission directly from the copyright holder. To view a copy of this licence, visit <http://creativecommons.org/licenses/by/4.0/>.

## References

- Bartos, D., Dunn, M., Sirignano, M., D'Anna, A., Masri, A.R.: Tracking the evolution of soot particles and precursors in turbulent flames using laser-induced emission. *Proc. Combust. Inst.* **36**(2), 1869 (2017). <https://doi.org/10.1016/j.proci.2016.07.092>

- Bhargava, A., Westmoreland, P.R.: MBMS analysis of a fuel-lean ethylene flame. *Combust. Flame* **115**(4), 456 (1998). [https://doi.org/10.1016/S0010-2180\(98\)00018-2](https://doi.org/10.1016/S0010-2180(98)00018-2)
- Boyette, W., Chowdhury, S., Roberts, W.: Soot particle size distribution functions in a turbulent non-premixed ethylene–nitrogen flame. *Flow Turbul. Combust.* **98**(4), 1173 (2017). <https://doi.org/10.1007/s10494-017-9802-5>
- Calcote, H.F.: Mechanisms of soot nucleation in flames—a critical review. *Combust. Flame* **42**(C), 215 (1981). [https://doi.org/10.1016/0010-2180\(81\)90159-0](https://doi.org/10.1016/0010-2180(81)90159-0)
- Cavaliere, D.E., Kariuki, J., Mastorakos, E.: A comparison of the blow-off behaviour of swirl-stabilized premixed, non-premixed and spray flames. *Flow Turbul. Combust.* **91**(2), 347 (2013). <https://doi.org/10.1007/s10494-013-9470-z>
- D’Anna, A.: Combustion-formed nanoparticles. In: *Proceedings of the Combustion Institute*, vol. 32, pp. 593–613. Elsevier Inc. (2009). <https://doi.org/10.1016/j.proci.2008.09.005>
- D’Anna, A., Rolando, A., Allouis, C., Minutolo, P., D’Alessio, A.: Nano-organic carbon and soot particle measurements in a laminar ethylene diffusion flame. In: *Proceedings of the Combustion Institute*, vol. 30, pp. 1449–1455 (2005). <https://doi.org/10.1016/j.proci.2004.08.276>
- D’Anna, A., Ciajolo, A., Alfè, M., Apicella, B., Tregrossi, A.: Effect of fuel/air ratio and aromaticity on the molecular weight distribution of soot in premixed n-heptane flames. In: *Proceedings of the Combustion Institute*, vol. 32, pp. 803–810 (2009). <https://doi.org/10.1016/j.proci.2008.06.198>
- Desgroux, P., Mercier, X., Thomson, K.A.: Study of the formation of soot and its precursors in flames using optical diagnostics. *Proc. Combust. Inst.* **34**(1), 1713 (2013). <https://doi.org/10.1016/j.proci.2012.09.004>
- Dockery, W.D., Pope III, C.A., Xu, X., Spengler, D.J., Ware, H.J., Fay, E.M., Ferris, G.B., Frank, E.S.: An association between air pollution and mortality in six U.S. cities. *N. Engl. J. Med.* **329**(24), 1753 (1993). <https://doi.org/10.1056/NEJM199307083290201>
- El Helou, I., Skiba, A.W., Mastorakos, E., Sidey, J.A.M.: Investigation of the effect of dilution air on soot production and oxidation in a lab scale rich–quench–lean (RQL) burner. In: *AIAA aerospace science meeting*, San Diego, California (2019). <https://doi.org/10.2514/6.2019-1436>
- Frenklach, M.: Reaction mechanism of soot formation in flames. *Phys. Chem. Chem. Phys.* **4**(11), 2028 (2002). <https://doi.org/10.1039/b110045a>
- Geigle, K.P., Schneider-Kühnle, Y., Tsurikov, M.S., Hadeff, R., Lücknerath, R., Krüger, V., Stricker, W., Aigner, M.: Investigation of laminar pressurized flames for soot model validation using SV-CARS and LII. In: *Proceedings of the Combustion Institute*, vol. 30, pp. 1645–1653 (2005). <https://doi.org/10.1016/j.proci.2004.08.158>
- Geigle, K.P., Zerbs, J., Kohler, M., Stohr, M., Meier, W.: Experimental analysis of soot formation and oxidation in a gas turbine model combustor using laser diagnostics. *J. Eng. Gas Turbines Power* **133**(12), 121503 (2011). <https://doi.org/10.1115/1.4004154>
- Geigle, K.P., Hadeff, R., Meier, W.: Soot formation and flame characterization of an aero-engine model combustor burning ethylene at elevated pressure. *J. Eng. Gas Turbines Power* **136**(2), 021505 (2013). <https://doi.org/10.1115/1.4025374>
- Geigle, K.P., Köhler, M., O’Loughlin, W., Meier, W.: Investigation of soot formation in pressurized swirl flames by laser measurements of temperature, flame structures and soot concentrations. *Proc. Combust. Inst.* **35**(3), 3373 (2015a). <https://doi.org/10.1016/j.proci.2014.05.135>
- Geigle, K.P., O’Loughlin, W., Hadeff, R., Meier, W.: Visualization of soot inception in turbulent pressurized flames by simultaneous measurement of laser-induced fluorescence of polycyclic aromatic hydrocarbons and laser-induced incandescence, and correlation to OH distributions. *Appl. Phys. B Lasers Opt.* **119**(4), 717 (2015b). <https://doi.org/10.1007/s00340-015-6075-3>
- Geigle, K.P., Hadeff, R., Stöhr, M., Meier, W.: Flow field characterization of pressurized sooting swirl flames and relation to soot distributions. In: *Proceedings of the Combustion Institute*, vol. 36, pp. 3917–3924. Elsevier Inc. (2017). <https://doi.org/10.1016/j.proci.2016.09.024>
- Geigle, K.P., Zerbs, J., Hadeff, R., Guin, C.: Laser-induced incandescence for soot measurements in an aero-engine combustor at pressures up to 20 bar. *Appl. Phys. B Lasers Opt.* **125**(6), 1 (2019). <https://doi.org/10.1007/s00340-019-7211-2>
- Giusti, A., Gkantonas, S., Foale, J.M., Mastorakos, E.: *Proceedings of the ASME Turbo Expo*, pp. 1–13 (2018). <https://doi.org/10.1115/GT2018-76705>
- Homann, K.H.: Fullerene and soot formation—aew pathways to large particles in flames. *Angew. Chem. Int. Ed. Engl.* **37**(18), 2435 (1998). [https://doi.org/10.1002/\(SICI\)1521-3773\(19981002\)37:18](https://doi.org/10.1002/(SICI)1521-3773(19981002)37:18)
- Houghton, J.T., Ding, Y., Griggs, D.J., Noguer, M., van der Linden, P.J., Dai, X., Maskell, K., Johnson, C.A.: *Climate Change 2001: The Scientific Basis. Contribution of Working Group I to the Third Assessment Report of the Intergovernmental Panel on Climate Change*. Cambridge University Press, Cambridge (2001). <https://doi.org/10.1256/004316502320517344>

- Karataş, A.E., Gülder, Ö.L.: Soot formation in high pressure laminar diffusion flames. *Prog. Energy Combust. Sci.* **38**(6), 818 (2012). <https://doi.org/10.1016/j.pecs.2012.04.003>
- Katsouyanni, K., Touloumi, G., Samoli, E., Gryparis, A., Le Tertre, A., Monopoli, Y., Rossi, G., Zmirou, D., Ballester, F., Boumghar, A., Anderson, H.R., Wojtyniak, B., Paldy, A., Braunstein, R., Pekkanen, J., Schindler, C., Schwartz, J.: Confounding and effect modification in the short-term effects of ambient particles on total mortality: results from 29 European cities within the APHEA2 project. *Epidemiology* **12**(5), 521 (2001). <https://doi.org/10.1097/00001648-200109000-00011>
- Köhler, M., Geigle, K.P., Meier, W., Crosland, B.M., Thomson, K.A., Smallwood, G.J.: Sooting turbulent jet flame: characterization and quantitative soot measurements. *Appl. Phys. B Lasers Opt. Phys.* **104**, 409 (2011). <https://doi.org/10.1007/s00340-011-4373-y>
- Lammel, O., Geigle, K.P., Luckerath, R., Meier, W., Aigner, M.: Investigation of soot formation and oxidation in a high-pressure gas turbine model combustor by laser techniques. In: *ASME Turbo Expo 2007: Power for Land, Sea and Air*, Montreal, Canada, pp. 1–8 (2007). <https://doi.org/10.1115/GT2007-27902>
- Mahmoud, S.M., Nathan, G.J., Alwahabi, Z.T., Sun, Z.W., Medwell, P.R., Dally, B.B.: The effect of exit strain rate on soot volume fraction in turbulent non-premixed jet flames. In: *Proceedings of the Combustion Institute*, vol. 36, pp. 889–897. Elsevier Inc. (2017). <https://doi.org/10.1016/j.proci.2016.08.055>
- Mahmoud, S.M., Nathan, G.J., Alwahabi, Z.T., Sun, Z.W., Medwell, P.R., Dally, B.B.: The effect of exit Reynolds number on soot volume fraction in turbulent non-premixed jet flames. *Combust. Flame* **187**, 42 (2018). <https://doi.org/10.1016/j.combustflame.2017.08.020>
- Michelsen, H.A.: Probing soot formation, chemical and physical evolution, and oxidation: a review of in situ diagnostic techniques and needs. In: *Proceedings of the Combustion Institute*, vol. 36, pp. 717–735. Elsevier Inc. (2017). <https://doi.org/10.1016/j.proci.2016.08.027>
- Narayanaswamy, V., Clemens, N.T.: Simultaneous LII and PIV measurements in the soot formation region of turbulent non-premixed jet flames. In: *Proceedings of the Combustion Institute*, vol. 34, pp. 1455–1463. The Combustion Institute (2013). <https://doi.org/10.1016/j.proci.2012.06.018>
- Penner, J.E., Zhang, S.Y., Chuang, C.C.: Soot and smoke aerosol may not warm climate. *J. Geophys. Res. D: Atmos.* **108**(21), AAC1 (2003). <https://doi.org/10.1029/2003JD003409>
- Pope III, C.A., Burnett, R.T., Thun, M.J., Calle, E.E., Krewski, D., Thurston, G.D.: Lung cancer, cardiopulmonary mortality, and long-term exposure to fine particulate air pollution. *J. Am. Med. Assoc.* **287**(9), 1132 (2002). <https://doi.org/10.1001/jama.287.9.1132>
- Qamar, N.H., Nathan, G.J., Alwahabi, Z.T., King, K.D.: The effect of global mixing on soot volume fraction: measurements in simple jet, precessing jet, and bluff body flames. In: *Proceedings of the Combustion Institute*, vol. 30, pp. 1493–1500. The Combustion Institute (2005). <https://doi.org/10.1016/j.proci.2004.08.102>
- Qamar, N.H., Alwahabi, Z.T., Chan, Q.N., Nathan, G.J., Roekaerts, D., King, K.D.: Soot volume fraction in a piloted turbulent jet non-premixed flame of natural gas. *Combust. Flame* **156**(7), 1339 (2009). <https://doi.org/10.1016/j.combustflame.2009.02.011>
- Quay, B., Lee, T.W., Ni, T., Santoro, R.J.: Spatially resolved measurements of soot volume fraction using laser-induced incandescence. *Combust. Flame* **97**(3–4), 384 (1994). [https://doi.org/10.1016/0010-2180\(94\)90029-9](https://doi.org/10.1016/0010-2180(94)90029-9)
- Richter, H., Howard, J.B.: Formation of polycyclic aromatic hydrocarbons and their growth to soot—a review of chemical reaction pathways. *Prog. Energy Combust. Sci.* **26**(4–6), 565 (2000). [https://doi.org/10.1016/S0360-1285\(00\)00009-5](https://doi.org/10.1016/S0360-1285(00)00009-5)
- Roussillo, M., Scoufflaire, P., Candel, S., Franzelli, B.: Experimental investigation of soot production in a confined swirled flame operating under perfectly premixed rich conditions. *Proc. Combust. Inst.* **37**(1), 893 (2018). <https://doi.org/10.1016/j.proci.2018.06.110>
- Samet, J., Dominici, F., Currier, F., Coursac, I., Zeger, S.: Fine particulate air pollution and mortality in 20 U.S. cities. *N. Engl. J. Med.* **343**(24), 1742 (2000). <https://doi.org/10.1056/NEJM200012143432401>
- Samuelsen, S.: Rich burn, quick-mix, lean burn (RQL) combustor. In: *The Gas Turbine Handbook*, pp. 227–233. U.S. Department of Energy (2006)
- Santoro, R.J., Semerjian, H.G.: Soot formation in diffusion flames: flow rate, fuel species and temperature effects. In: *Symposium (International) on Combustion*, vol. 20, pp. 997–1006 (1985). [https://doi.org/10.1016/S0082-0784\(85\)80589-0](https://doi.org/10.1016/S0082-0784(85)80589-0)
- Santoro, R.J., Semerjian, H.G., Dobbins, R.A.: Soot particle measurements in diffusion flames. *Combust. Flame* **51**, 203 (1983). [https://doi.org/10.1016/0010-2180\(83\)90099-8](https://doi.org/10.1016/0010-2180(83)90099-8)

- Santoro, R.J., Yeh, T.T., Horvath, J.J., Semerjian, H.G.: The transport and growth of soot particles in laminar diffusion flames. *Combust. Sci. Technol.* **53**(2–3), 89 (1987). <https://doi.org/10.1080/00102208708947022>
- Shaddix, C.R., Smyth, K.C.: Laser-induced incandescence measurements of soot production in steady and flickering methane, propane, and ethylene diffusion flames. *Combust. Flame* **107**(4), 418 (1996). [https://doi.org/10.1016/S0010-2180\(96\)00107-1](https://doi.org/10.1016/S0010-2180(96)00107-1)
- Singh, P., Sung, C.J.: PAH formation in counterflow non-premixed flames of butane and butanol isomers. *Combust. Flame* **170**, 91 (2016). <https://doi.org/10.1016/j.combustflame.2016.05.009>
- Singh, P., Hui, X., Sung, C.J.: Soot formation in non-premixed counterflow flames of butane and butanol isomers. *Combust. Flame* **164**, 167 (2016). <https://doi.org/10.1016/j.combustflame.2015.11.015>
- Sirignano, M., Conturso, M., Magno, A., Di Iorio, S., Mancarusò, E., Vaglieco, B.Maria, D'Anna, A.: Evidence of sub-10 nm particles emitted from a small-size diesel engine. *Exp. Therm. Fluid Sci.* **95**, 60 (2018). <https://doi.org/10.1016/j.expthermfluidsci.2018.01.031>
- Smyth, K.C., Miller, J.H., Dorfman, R.C., Mallard, W.G., Santoro, R.J.: Soot inception in a methane/air diffusion flame as characterized by detailed species profiles. *Combust. Flame* **62**(2), 157 (1985). [https://doi.org/10.1016/0010-2180\(85\)90143-9](https://doi.org/10.1016/0010-2180(85)90143-9)
- Steinmetz, S.A., Fang, T., Roberts, W.L.: Soot particle size measurements in ethylene diffusion flames at elevated pressures. *Combust. Flame* **169**, 85 (2016). <https://doi.org/10.1016/j.combustflame.2016.02.034>
- Stöhr, M., Geigle, K.P., Hedef, R., Boxx, I., Carter, C.D., Grader, M., Gerlinger, P.: Time-resolved study of transient soot formation in an aero-engine model combustor at elevated pressure. In: Proceedings of the Combustion Institute, vol. 37, pp. 5421–5428 (2019). <https://doi.org/10.1016/j.proci.2018.05.122>
- Syred, N.: A review of oscillation mechanisms and the role of the precessing vortex core (PVC) in swirl combustion systems. *Prog. Energy Combust. Sci.* **32**, 93 (2006). <https://doi.org/10.1016/j.pecs.2005.10.002>
- Syred, N., Beer, J.M.: Combustion in swirling flows : a review. *Combust. Flame* **23**(2), 143 (1974). [https://doi.org/10.1016/0010-2180\(74\)90057-1](https://doi.org/10.1016/0010-2180(74)90057-1)
- Tracy, T., Sidey, J.A.M., Mastorakos, E.: A lab-scale rich–quench–lean (RQL) combustor for stability and soot investigations. In: AIAA aerospace science meeting, Kissimmee, Florida (2018). <https://doi.org/10.2514/6.2018-1880>
- Tsurikov, M.S., Geigle, K.P., Krüger, V., Schneider-Kühnle, Y., Stricker, W., Lücknerath, R., Hedef, R., Aigner, M.: Laser-based investigation of soot formation in laminar premixed flames at atmospheric and elevated pressures. *Combust. Sci. Technol.* **177**(10), 1835 (2005). <https://doi.org/10.1080/00102200590970212>
- Vander Wal, R.L., Jensen, K.A., Choi, M.Y.: Simultaneous laser-induced emission of soot and polycyclic aromatic hydrocarbons within a gas-jet diffusion flame. *Combust. Flame* **109**(3), 399 (1997). [https://doi.org/10.1016/S0010-2180\(96\)00189-7](https://doi.org/10.1016/S0010-2180(96)00189-7)
- Wang, H.: Formation of nascent soot and other condensed-phase materials in flames. In: Proceedings of the Combustion Institute, vol. 33, pp. 41–67. Elsevier Inc. (2011). <https://doi.org/10.1016/j.proci.2010.09.009>
- Wang, G.H., Clemens, N.T.: Effects of imaging system blur on measurements of flow scalars and scalar gradients. *Exp. Fluids* **37**(2), 194 (2004). <https://doi.org/10.1007/s00348-004-0801-7>
- Wang, L., Chatterjee, S., An, Q., Steinberg, A.M., Gülder, Ö.L.: Soot formation and flame structure in swirl-stabilized turbulent non-premixed methane combustion. *Combust. Flame* **209**, 303 (2019a). <https://doi.org/10.1016/j.combustflame.2019.07.033>
- Wang, L.Y., Bauer, C.K., Gülder, Ö.L.: Soot and flow field in turbulent swirl-stabilized spray flames of Jet A-1 in a model combustor. In: Proceedings of the Combustion Institute, vol. 37, pp. 5437–5444. Elsevier Inc. (2019b). <https://doi.org/10.1016/j.proci.2018.05.093>